Appendix A. Acquisition and reconstruction

CBCT scans were reconstructed using the FDK algorithm [31]. The USC was primarily developed for portal dosimetry [18]. The projection images are corrected by subtracting uniform scatter, which is assumed to be a fraction S_f of the mean intensity $\bar{I}$ of the projection images of the unattenuated part of the beam:

$$I_{corrected} = I_{uncorrected} - S_f \bar{I}_{uncorrected}$$

If applicable, S_f was adapted to the use of an ASG by decreasing it from 0.24 to 0.045. XVI has also been enhanced with an iterative scatter correction (ISC), which determined the scatter contribution for each pixel individually [19, 32]. The USC and ISC potentially resulted in local overestimations of scatter and negative pixel values, which needed to be corrected before the log-transformation of the data. In case of the USC this was performed by shifting the pixel values so that the minimum value was equal to a pre-defined low value, which we set to 20. For the ISC a pixel-based non-negativity correction adapted from work of Xu et al. [33] was implemented. This method modifies the scatter estimation as a function of the scatter-to-total ratio (STR) using a linear part below a pre-defined STR threshold and a curve asymptotically approaching unity for STR $\rightarrow \infty$. We empirically chose threshold values between 0.3 and 0.5 depending on the pixel value. Finally, a polynomial beam hardening correction was applied. The pixel-based non-negativity and the beam hardening correction were only applied with the ISC to compare the combination of all currently available corrections with the commercially available version (Elekta standard setting). For the USC and ISC an image lag correction was applied [34].

Table A.1. Acquisition parameters. The acquisitions were performed with 120 kV.

Site	mA	ms	Field-of-view	Gantry speed
Head and neck	16	40	MFOV	360°/min
Lung	16	40	SFOV	180°/min
Pelvic region	32	40	MFOV	180°/min
Prostate	32	40	MFOV	180°/min

Appendix B. Calibration

The importance of site specific HU and PD calibrations can be seen in the dose volume histograms (DVH) for the Alderson phantom (Fig. B.1). It is visible that the agreement between pCT and CBCT is better with a site specific calibration than with one designated for another site, especially in high dose areas and the pelvic region. The effect is stronger for the USC than for the ISC.

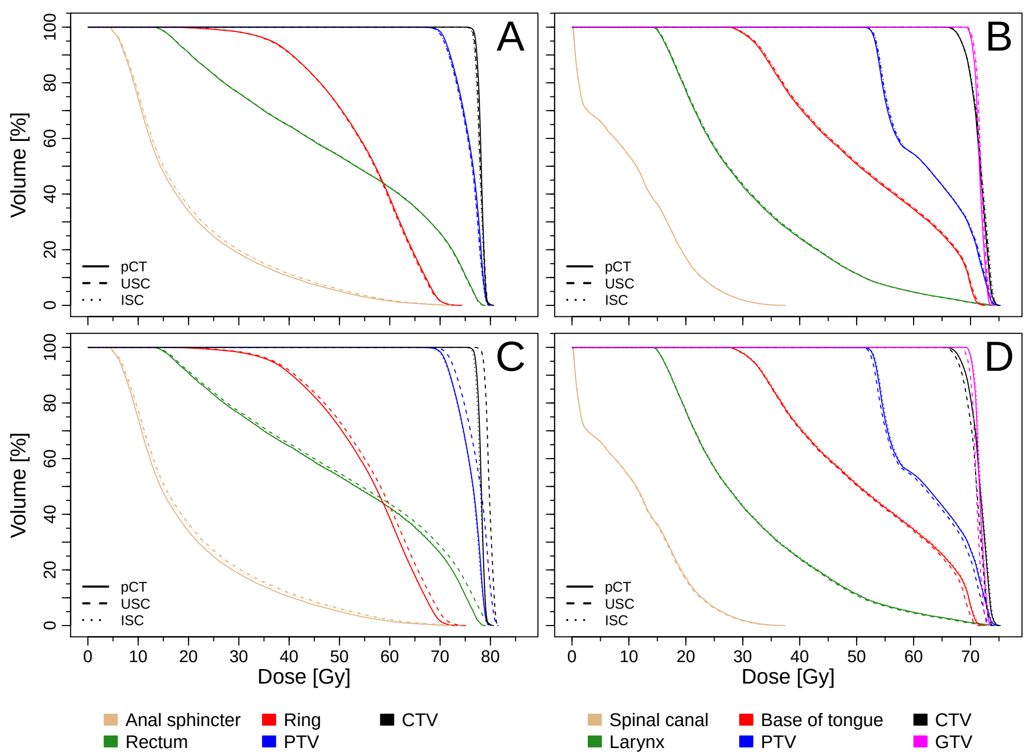

Fig. B.1. Dose volume histograms of the Alderson phantom for the pelvic region (A, C) and H&N (B, D). A and B show the results when an appropriate site specific calibration was used, i.e., the CIRS pelvis configuration for the pelvic plan and the CIRS H&N configuration for the Alderson H&N plan. C and D show the use of the opposing calibration, i.e., the CIRS pelvis configuration for the H&N plan and the CIRS H&N configuration for the pelvic plan.

For the calibration the CT Number Linearity and density inserts of the CIRS phantom were used. Volumes of interest were placed in the scans and the mean values were determined. These mean values were used as data points for the CBCT number (Fig. B.2) and HU (Fig. B.3).

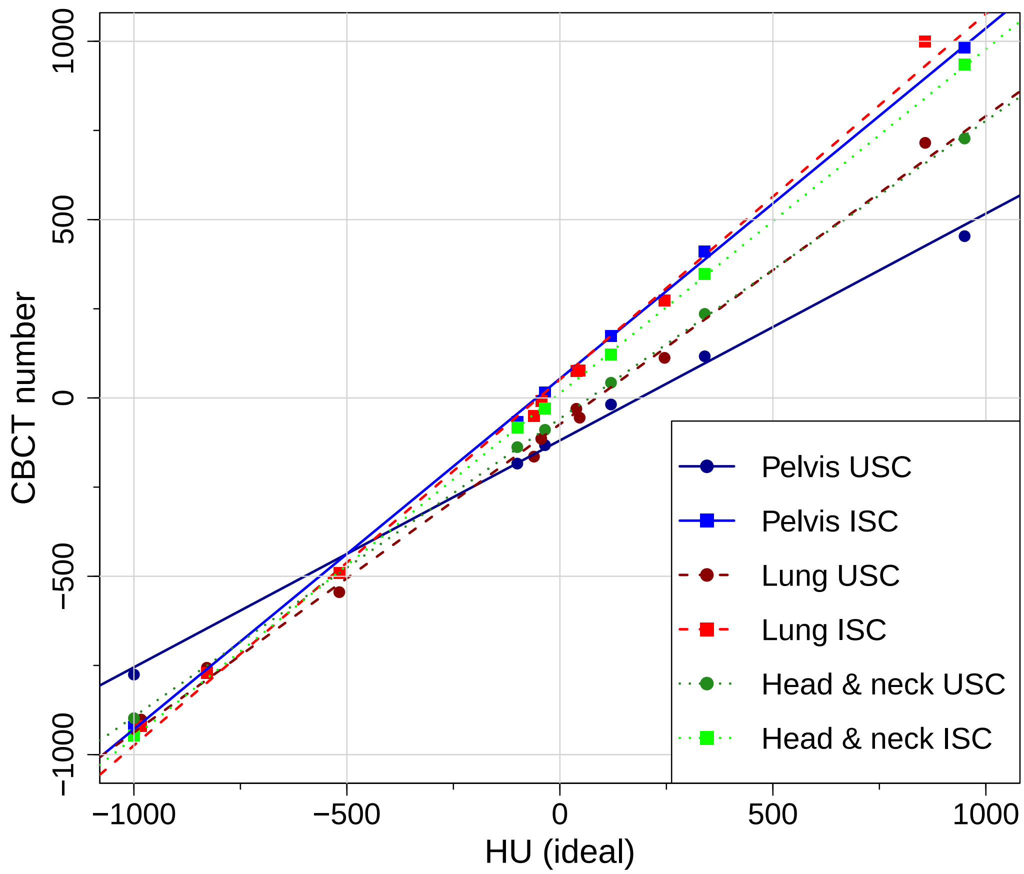

Fig. B.2. HU calibration for the uniform (USC) and iterative scatter correction (ISC) both with ASG. The data points represent the phantom inserts and the lines the linear regression. The parameters of the linear regressions are presented in Table B.1.

Even with a site specific HU calibration, differences between the HU-PD curves of the imaging sites were still present, making also a site specific calibration for the HU-PD relation necessary (Fig. B.3).

Table B.1. Parameters of the regressions from Fig. B.2.

Site	Intercept	Slope	R^2
Pelvis USC	-119.19	0.636	0.9970
Pelvis ISC	53.94	0.983	0.9994
Lung USC	-73.70	0.864	0.9963
Lung ISC	51.43	1.026	0.9962
Head & neck USC	-58.21	0.835	0.9999
Head & neck ISC	13.25	0.965	0.9999

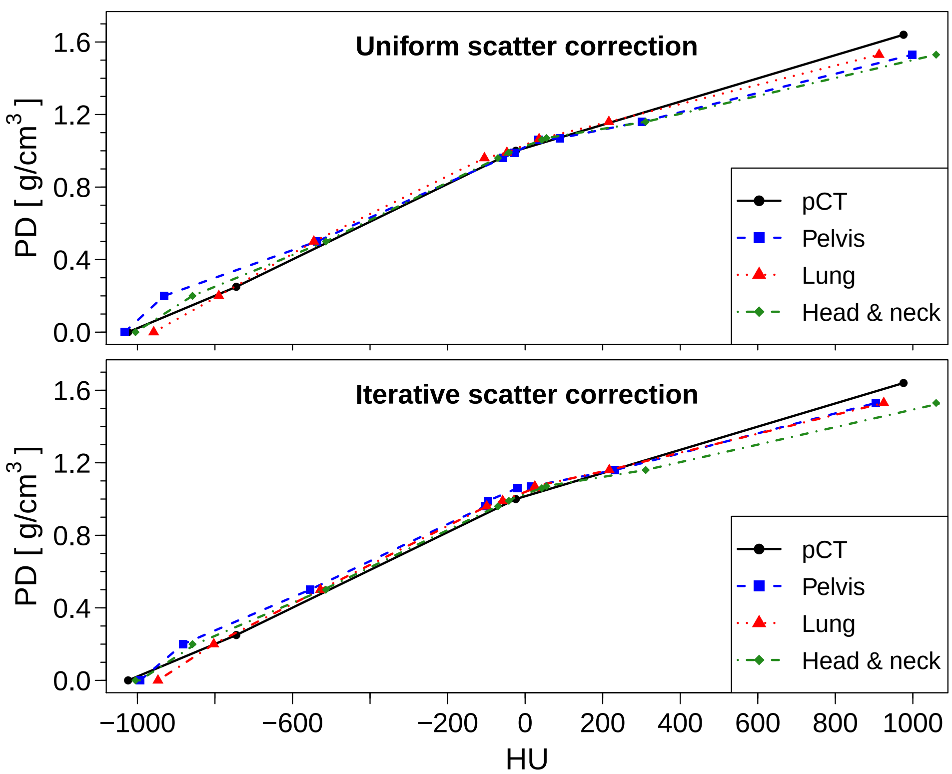

Fig. B.3. Hounsfield unit (HU) - physical density (PD) calibration curves for the uniform (USC) and iterative scatter correction (ISC). For both methods the same pCT curve and the three CBCT curves of the site specific phantom configurations simulating the treatment sites are shown.

Appendix C. Phantom results

Table C.1. Mean relative dose difference for the phantom plans of the three imaging sites for uniform and iterative scatter correction for the volume enclosed by the 50 % isodose surface. The results are shown with one standard deviation.

Site	USC w/ ASG [%]	ISC w/ ASG [%]	USC w/o ASG [%]
Head & Neck	0.6 ± 0.7	0.7 ± 0.8	1.9 ± 8.0
Lung	0.6 ± 0.6	0.8 ± 0.8	0.8 ± 0.7
Pelvic region	0.8 ± 0.7	0.9 ± 0.7	3.9 ± 1.4
Prostate	1.9 ± 1.1	0.9 ± 0.7	2.5 ± 1.2

Appendix D. Dose-volume histograms

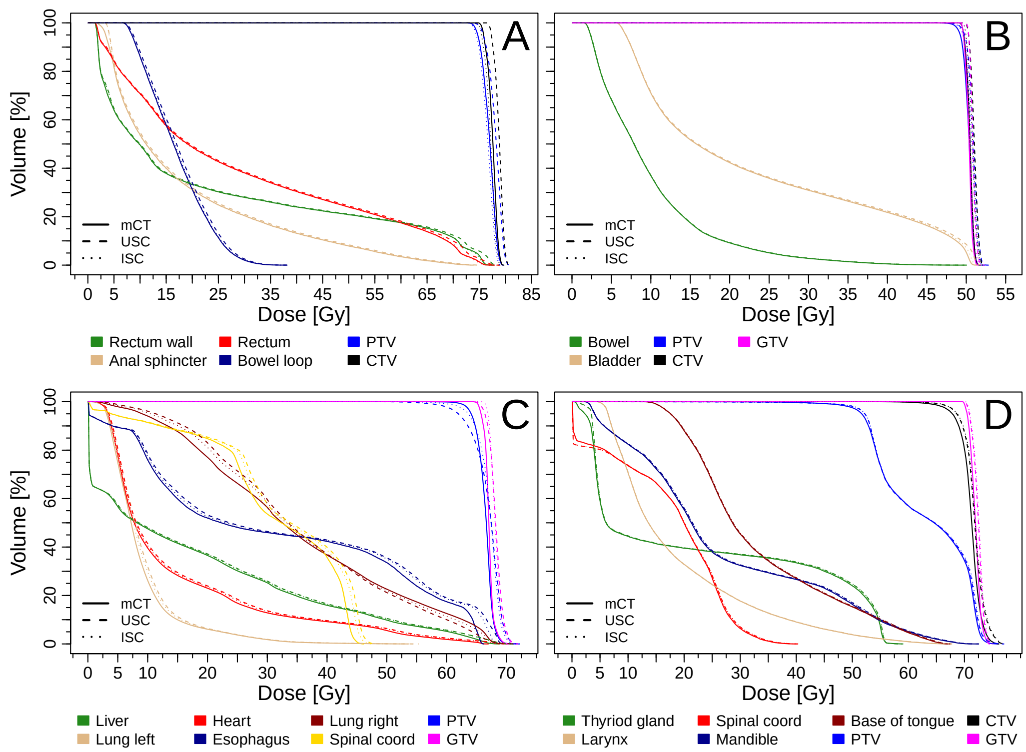

Fig. D.1. Dose-volume histograms for one prostate (A), pelvic region (rectum) (B), lung (C), and head and neck (D) patient. Only one mCT is shown because of no visible difference between the mCT for USC and ISC. The chosen patients are from cohort 1 and have metric values close to the median of their group.

References

[31] Feldkamp LA, Davis LC, Kress JW. Practical cone-beam algorithm. J Opt Soc Am 1984;:612–619.

[32] Stankovic U, van Herk M, Ploeger LS, Sonke JJ. Improved image quality of cone beam CT scans for radiotherapy image guidance using fiber-interspaced antiscatter grid. Med Phys 2014;41:061910.

[33] Xu Y, Bai T, Yan H, Ouyang L, Pompos A, Wang J, et al. A practical cone-beam CT scatter correction method with optimized Monte Carlo simulations for image-guided radiation therapy. Phys Med Biol 2015;60:3567–3587.

[34] Stankovic U, Ploeger LS, Sonke JJ, van Herk M. Clinical introduction of image lag correction for a cone beam CT system. Med Phys 2016;43:1057–1064.